RESEARCH ARTICLE | MARCH 02 2026

Surface morphology control of the Cassie–Wenzel transition: An energy landscape perspective

Lisen Bi ; Fei Wang ; Britta Nestler

J. Chem. Phys. 164, 094701 (2026)
https://doi.org/10.1063/5.0303819

The Journal of Chemical Physics ARTICLE pubs.aip.org/aip/jcp

Surface morphology control of the Cassie–Wenzel transition: An energy landscape perspective

Cite as: J. Chem. Phys. 164, 094701 (2026); doi: 10.1063/5.0303819
Submitted: 24 September 2025 • Accepted: 11 February 2026 •
Published Online: 2 March 2026

Lisen Bi,[1] Fei Wang,[1,2,a)] and Britta Nestler[1,2,3]

AFFILIATIONS

[1] Institute for Applied Materials - Microstructure Modelling and Simulation (IAM-MMS), Karlsruhe Institute of Technology (KIT), Strasse am Forum 7, 76131 Karlsruhe, Germany
[2] Institute of Nanotechnology (INT), Karlsruhe Institute of Technology (KIT), Hermann-von-Helmholtz-Platz 1, 76344 Eggenstein-Leopoldshafen, Germany
[3] Institute of Digital Materials Science, Karlsruhe University of Applied Sciences, Moltkestrasse 30, 76133 Karlsruhe, Germany

[a)] **Author to whom correspondence should be addressed:** fei.wang@kit.edu

ABSTRACT

Surface morphology is widely recognized to influence wetting behavior; however, a comprehensive understanding of how specific morphological factors govern the Cassie–Wenzel transition remains incomplete. In this work, building on a bivariate energy-minimization framework, we focus on a key structural design parameter characterizing individual surface defects and systematically investigate its effect—both independently and in conjunction with surface defect density—on three critical aspects of the Cassie–Wenzel transition: wettability, energy barrier, and static friction. Our results demonstrate that this structural design parameter exerts distinct influences on the Cassie–Wenzel transition, depending on the wetting type: in type A, the Wenzel state is energetically favored, while in type B, the Cassie state represents the global energy minimum. These findings reveal that this parameter modulates the stability and reversibility of wetting states, as well as droplet mobility, through nontrivial energy landscapes. Moreover, we uncover a previously unreported non-monotonic dependence of static friction on the morphological factors, which we attribute to a geometric constraint on the contact angle of the transition state. We anticipate that our findings can offer quantitative design guidelines for engineering surfaces with tunable wettability and droplet transport properties.

I. INTRODUCTION

Wetting phenomena on rough hydrophobic surfaces are central to both natural processes and technological applications,[1] governing behaviors such as self-cleaning,[2] water collection,[3] and fluid transport.[4] Unlike ideal smooth surfaces, rough surfaces introduce geometric complexities that significantly alter liquid behavior, leading to unique wetting states and transitions. These phenomena are often described by the Cassie–Wenzel theory[5,6] (CWT), which extends the classical Young's equation[7] by incorporating the effects of surface roughness on the solid–fluid interfaces.

CWT has been instrumental in describing wetting on rough hydrophobic surfaces by introducing two distinct states: the Cassie state [Fig. 1(a)], where droplets sit atop air pockets trapped within surface asperities, and the Wenzel state [Fig. 1(b)], where the liquid fully wets the rough surfaces. These states are mathematically expressed as[8]

$$\cos\theta_W = \Upsilon \cos\theta_Y, \tag{1}$$

$$\cos\theta_C = \Phi \cos\theta_Y - (1 - \Phi), \tag{2}$$

where θ_W and θ_C represent the apparent contact angles of the droplet in the Wenzel state and Cassie state, respectively. Υ is the roughness factor, defined as the ratio of the actual liquid–solid area to the projected area. Φ is the solid fraction, i.e., the fraction of the solid surface in contact with the liquid beneath the droplet. θ_Y is the equilibrium Young's contact angle, which characterizes the wetting behavior on an ideal, flat surface. This theoretical framework provides a robust foundation for understanding wetting behavior on real-world surfaces. Importantly, CWT serves as a guiding principle for designing functional hydrophobic surfaces, such as superhydrophobic coatings,[9] self-cleaning materials,[10] and microfluidic devices.[11] However, it often oversimplifies wetting phenomena by neglecting the intermediate states [Fig. 1(c)] between the Cassie and

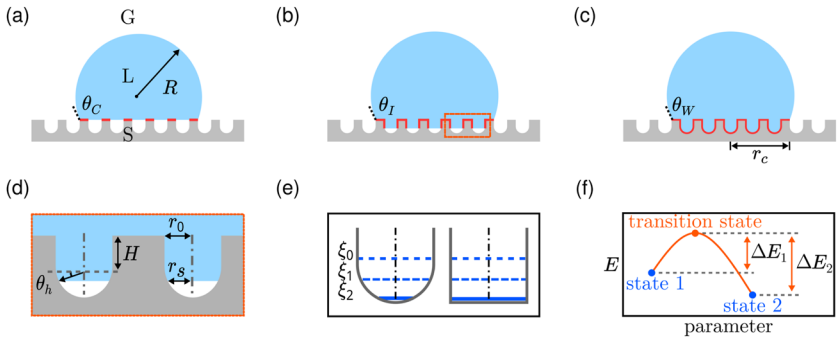

FIG. 1. Schematic cross-sectional illustration depicting various wetting states of a sessile droplet on a rough hydrophobic surface: (a) Cassie state, (b) intermediate state, and (c) Wenzel state. G, L, and S represent the gas, liquid, and solid, respectively. The red lines emphasize the variation in actual liquid–solid contact area across the different states. (d) Enlarged view of the orange dashed box in (b), showing the partial infiltration of liquid into hydrophobic surface defects. (e) Sketch of the time evolution of the liquid–gas interface (blue lines) progressing downward within the surface defect at various infiltration levels, ξ_0, ξ_1, and ξ_2: a progressive retreat in our structure (left), contrasted with an abrupt collapse in the conventional geometry (right). (f) Schematic illustration of the energy barrier during the Cassie–Wenzel transition on hydrophobic surfaces.

Wenzel states, as well as the transitions among them, collectively referred to as the Cassie–Wenzel transition.[12–14]

The Cassie–Wenzel transition on hydrophobic surfaces refers to the process by which droplets shift between the Cassie state and the Wenzel state. Instead of a direct or instantaneous shift, it typically unfolds through a series of intermediate states, in which partial wetting coexists with trapped air pockets or re-emerging air cavities [Fig. 1(d)]. Such behavior plays a critical role in elucidating the stability, reversibility, and hysteresis of wetting behavior, which are key factors that underpin practical applications such as switchable wettability,[15,16] antifouling coatings,[17] and controlled fluid transport.[18] However, despite its importance, this transition remains poorly understood.

Currently, the micro- and nanoscale nature of liquid–gas interface evolution during the transition presents a major challenge for the direct experimental observation and characterization of intermediate states. However, recent advances in imaging and characterization techniques have enabled remarkable progress in this field.[19–23] Notably, Lv *et al.*[20] utilized confocal microscopy to dynamically observe and quantitatively characterize metastable states during the Cassie–Wenzel transition on submerged superhydrophobic surfaces, revealing a diffusion-dominated mechanism of air pocket dissipation. Complementing the experimental breakthroughs, atomistic simulations, particularly molecular dynamics (MD), have significantly advanced our understanding of the transition at the nanoscale by uncovering microscopic mechanisms that govern the process, e.g., liquid–solid interactions, which give rise to interfacial energy.[24–28] By offering micro-level resolution, these simulations have enabled researchers to systematically investigate how critical parameters—such as temperature, pressure, and surface geometry—influence the stability of both Cassie and Wenzel states.

Despite significant progress, both experimental and computational approaches have yet to capture the transition across multiple scales. Experimentally, efforts have predominantly focused on liquid–gas interfaces confined within surface defects, without extending their scope to simultaneously observe multiscale interfaces. Although atomic simulations have explored these phenomena, the simulated droplet sizes are typically comparable to the scale of micro-/nano-roughness, failing to replicate the substantial size disparity observed in real-world systems, where droplet sizes and surface roughness span orders of magnitude. Extending these simulations to macroscopic droplet sizes on submicrometer-rough surfaces, even with high-performance supercomputers, would require computational times spanning months or even years.

Models grounded in energy minimization principles offer a promising framework for achieving a multi-scale nature. By expressing the total free energy as a combination of liquid–solid, liquid–gas, and solid–gas interfacial energies, along with gravitational and capillary effects, such models have been used to calculate the potential barrier separating wetting states.[29–31] However, early implementations still exhibit inherent constraints similar to the classical CWT. An alternative approach, based on the calculation of the normalized depinning force along the unit length of the three-phase contact line, gives rise to the so-called 1D Cassie–Wenzel transition,[32] which is generally limited to systems that can be approximated along a single spatial dimension.

To overcome these limitations, we previously extended the conventional energy minimization framework by introducing an additional degree of freedom, ξ, defined as the effective liquid–solid contact fraction as the droplet gradually invades or recedes from the hydrophobic surface defects.[33] This generalized framework enables the construction of a continuous energy landscape that seamlessly connects the Cassie state, the Wenzel state, and all intermediate states. As such, it provides a unified description of the Cassie–Wenzel transition on hydrophobic surfaces. However, our prior work focused on elucidating the structure of the energy landscape under the assumption of a fixed morphology for individual defects to isolate the essential physics of this transition. As a consequence, how variations in individual defect morphology influence this transition remains unresolved. To address this open question, building upon our previous theoretical framework, the present work undertakes a necessary and systematic parametric investigation to clarify how individual defect morphology affects the Cassie–Wenzel transition on hydrophobic surfaces across three crucial aspects: wettability, energy barrier, and static friction. In addition, we

further explore the nonlinear interplay between distinct morphological factors modulating the transition behavior along these same dimensions. In doing so, we broaden the practical applicability of the Cassie–Wenzel transition theory and bridge the gap between theoretical insights and application-oriented surface engineering, offering design guidelines for tailoring wetting behavior through controlled manipulation of surface features.

II. THEORETICAL METHODS

A. Energy-based wetting model with dual variables

For a droplet with volume $V = 4\pi R_0^3/3$ (R_0 is an imaginary sphere radius) and a Bond number $\mathrm{Bo} = \rho R_0^2 g/\gamma_{lg}$ (ρ is the density of the droplet, g is the gravity acceleration, and γ_{lg} is the liquid–gas interfacial tension) much less than unity, both the gradual penetration into and retraction from surface defects—whose characteristic features are much smaller than the droplet radius R—that is, the Cassie–Wenzel transition, can be accurately captured by the bivariate energy minimization model we previously proposed.[33] A key advantage of our model is its ability to accurately track liquid–gas interfaces across multiple length scales simultaneously.

In our model, a parameter representing the effective liquid–solid contact ratio, ξ, is introduced to scrutinize the continuous wetting transition process. This parameter is defined as

$$\xi = \frac{S_t}{\pi(R\sin\theta)^2}, \tag{3}$$

where S_t is the true liquid–solid contact area, which increases as the liquid progressively wets the underlying surface defects, and θ is the apparent contact angle of the droplet. The parameter ξ quantifies the evolution of the liquid–solid contact area during the Cassie–Wenzel transition, with the projected base area of the droplet, $\pi(R\sin\theta)^2$, serving as the reference. Physically, this parameter can be interpreted as an indicator of the extent to which the liquid infiltrates the surface defects:

- I ($\xi = \xi_{\min}$): The liquid barely contacts the surface defects [Fig. 1(a)(i)], representing the Cassie state.
- II ($\xi_{\min} < \xi < \xi_{\max}$): Both liquid–solid contact and trapped air coexist beneath the droplet [Fig. 1(a)(ii)], indicating the continuous Cassie–Wenzel transition process.
- III ($\xi = \xi_{\max}$): The liquid completely fills the surface defects [Fig. 1(a)(iii)], corresponding to the Wenzel state.

Our model introduces ξ as a free variable, which allows the total interfacial energy of the system to be formulated as a function of both θ and ξ. By minimizing the interfacial energy with respect to these two variables, rather than only with respect to θ, we obtain a complete energy landscape $E(\theta, \xi)$ that spans the entire transition from the Cassie state to the Wenzel state. Similar energy approaches have been developed in previous studies, such as Ref. 24. Here, however, ξ is directly linked to the macroscopic geometry of surface defects, enabling a systematic examination of how the Cassie–Wenzel transition varies with structural parameters. It should be noted that this two-dimensional formulation, which relies only on θ and ξ, captures the transition between the Cassie and Wenzel states but does not include all possible wetting states. As pointed out in the works,[34,35] a Cassie-impregnating state may also occur. Describing such a state requires an additional degree of freedom, β, to characterize local infiltration into individual surface defects located outside the droplet's contact region, which leads to a 3D energy map, $E(\theta, \xi, \beta)$. Such a refinement shows a higher dimensional energy map that exceeds the scope of the present two-variable description.

A critical requirement of our model is the differentiability of the interfacial energy with respect to θ and ξ. To ensure this, two physically motivated assumptions are considered. First, the liquid–gas interface within the surface defects is assumed to be flat. Second, the surface defects, characterized by an average radius, r_0, are modeled as three-dimensional holes with cylindrical cavities of height H smoothly connected to hemispherical bottoms [see Fig. 1(d)]. These assumptions are not introduced solely for analytical tractability; rather, they ensure that the total interfacial energy varies smoothly throughout the transition between the Cassie state and the Wenzel state. In other words, they preserve the intrinsic differentiability of the energy landscapes associated with the Cassie–Wenzel transition, in contrast to the first-order wetting transition that exhibits discontinuities in interfacial energy.[36,37]

With the variables and assumptions established, the free energy of the whole system can be described by the total interfacial energy as

$$E = \gamma_{lg}A_0 + (\gamma_{sl} - \gamma_{sg})S_t + \gamma_{lg}\sum_{i=1}^{n} A_i + C. \tag{4}$$

Here, γ_{sl} and γ_{sg} represent the interfacial tensions of the solid–liquid and solid–gas interfaces. The first term denotes the liquid–gas interfacial energy of the droplet's spherical cap with area A_0. The second term denotes the net interfacial energy change resulting from the replacement of the solid–gas interface by the solid–liquid interface as the liquid spreads over the surface. The third term denotes the cumulative liquid–gas interfacial energy formed within the surface defects, where A_i is the area of the liquid–gas interface inside the i-th defect and the summation runs over all n wet defects. The constant term C originates from the solid–gas interfacial energy associated with the total surface area. Since this area is fixed for a given surface geometry and γ_{sg} is taken as an intrinsic property of the solid–gas pair under constant temperature, C does not influence the equilibrium condition obtained from energy minimization and can be absorbed into the reference energy. Therefore, neglecting C in the subsequent derivations does not affect the physical meaning or validity of the results. If changes in γ_{sg} lead to variations in C that affect the equilibrium state, we refer to Ref. 38 for a detailed discussion.

To further simplify the expression, we assume that the surface defects are distributed with an average density ρ_s, defined as

$$\rho_s = \frac{n}{\pi(R\sin\theta)^2}, \tag{5}$$

where n is the number of defects distributed over the droplet base area $\pi(R\sin\theta)^2$. The parameter ρ_s quantifies the number of defects per unit area (in units of mm^{-2}) and characterizes the macroscopic surface roughness: a nonzero value ($\rho_s > 0$) indicates the presence of structural defects on the surface, whereas $\rho_s = 0$ corresponds to an atomically smooth surface. Thus, ρ_s can be regarded as one of the

key distinct morphological factors. Under the assumption of ρ_s, the total number of defects wetted by the droplet can be approximated as $n = \rho_s \pi (R \sin\theta)^2$. Correspondingly, the minimum and maximum effective liquid–solid contact ratios take the closed forms as

$$\xi_{\min} = 1 - \rho_s \pi r_0^2, \tag{6}$$

$$\xi_{\max} = 1 + \rho_s \pi r_0^2 [2(H/r_0) + 1], \tag{7}$$

and the summation term in Eq. (4) that accounts for the liquid–gas interfacial area inside the defects becomes

$$\sum_{i=1}^{n} A_i = \pi r_s^2 \rho_s \pi (R \sin\theta)^2. \tag{8}$$

Here, r_s is the radius of the liquid–gas interface within an individual surface defect [Fig. 1(d)]. The value of r_s depends on the vertical position of the meniscus within the defect geometry: when the interface is located within the cylindrical portion of the defect, $r_s = r_0$; when the interface lies within the hemispherical cap, $r_s = r_0 \cos\theta_h$, where θ_h is the angle between the line connecting the triple point on the interface edge to the center of the hemispherical cap and the horizontal base of the hemisphere. From Eq. (3), θ_h and ξ are related by

$$\sin\theta_h = \frac{1}{2}\left(\frac{\xi - 1}{\rho_s \pi r_0^2} - 2\frac{H}{r_0} + 1\right). \tag{9}$$

It then follows that r_s varies with ξ according to

$$r_s = r_0 \cos\theta_h(\xi) = r_0\sqrt{1 - \sin^2\theta_h(\xi)}. \tag{10}$$

As ξ increases toward $\xi_{\max}$, θ_h reaches 90° and r_s becomes zero, indicating that the liquid–gas interface beneath the droplet disappears in the fully wet (Wenzel) state [see Fig. 1(e)].

To proceed, we incorporate the geometric constraints of a droplet with fixed volume, which is assumed to retain a spherical-cap shape throughout the transition. This assumption originates from two physical conditions: first, $Bo \ll 1$, indicating that surface tension dominates over gravity; second, the characteristic size of the surface defects is much smaller than the droplet radius, ensuring that the volume of liquid penetrating into the defects is negligible compared to the total droplet volume. Under the fixed-volume constraint, the volume V and surface area A_0 of the droplet are given by the standard geometric relations,[39,40]

$$V = \frac{\pi}{3} R^3 (2 + \cos\theta)(1 - \cos\theta)^2 \tag{11}$$

and

$$A_0 = 2\pi R^2 (1 - \cos\theta). \tag{12}$$

By substituting Eqs. (3), (8), (11), and (12) into the energy function of Eq. (4) and applying the well-known Young's equation $\gamma_{sg} - \gamma_{sl} = \gamma_{lg}\cos\theta_Y$, the total interfacial energy of the system can be written as

$$\frac{E}{\gamma_{lg}\left(3V\sqrt{\pi}\right)^{2/3}} = \frac{2 - (1 + \cos\theta)\left(\xi\cos\theta_Y - \rho_s \pi r_s^2\right)}{(1 - \cos\theta)^{1/3}(2 + \cos\theta)^{2/3}}. \tag{13}$$

Since both V and γ_{lg} are constant in our model, they do not affect the equilibrium condition derived from the energy minimization. Therefore, for convenience in the subsequent analysis, we define a dimensionless form of the total interfacial energy as

$$\tilde{E} = \frac{E}{\gamma_{lg}\left(3V\sqrt{\pi}\right)^{2/3}}. \tag{14}$$

This dimensionless formulation allows us to systematically investigate how θ and ξ jointly influence the total interfacial energy. In particular, it provides a natural basis for visualizing the energy landscape associated with the Cassie–Wenzel transition. To verify the validity of our energy function, we compare its limiting form with the exact expression of the total interfacial energy in the fully wet (Wenzel) state reported in Ref. 41. Substituting $\xi = \xi_{\max}$ into Eq. (13) and using the normalization defined in Eq. (14), we obtain

$$\tilde{E}_W = \frac{2 - \xi_{\max}\cos\theta_Y(1 + \cos\theta_W)}{(1 - \cos\theta_W)^{1/3}(2 + \cos\theta_W)^{2/3}}. \tag{15}$$

Based on the definition in Eq. (3), $\xi_{\max}$ corresponds to the roughness factor Υ. By further applying Eq. (1), Eq. (15) simplifies to

$$\tilde{E}_W = (1 - \cos\theta_W)^{2/3}(2 + \cos\theta_W)^{1/3}, \tag{16}$$

which coincides with the theoretical expression for the Wenzel state in Ref. 41. This consistency confirms the accuracy of the present energy function.

In addition to ρ_s, our model includes another key distinct morphological factor that characterizes the morphology of individual defects: the structural design parameter, H/r_0, where H is the height of the cylindrical part of the surface defect [Fig. 1(d)]. This dimensionless ratio serves as a vertical descriptor of defect geometry, effectively capturing the "depth" of individual defects relative to their lateral scale. The geometric profile of each defect, characterized by H/r_0, determines the maximum achievable liquid–solid contact area during the wetting transition process. By setting the accessible range of ξ [see Eq. (7)], H/r_0 directly enters the total interfacial energy formulation. Consequently, variations in H/r_0 indirectly shape the energy landscape and influence the Cassie–Wenzel transition. Along with ρ_s, these effects will be quantitatively analyzed in Sec. III.

By systematically sampling the dimensionless energy function over a sufficiently fine and uniformly spaced grid within the domain,

$$\Lambda = \left\{(\theta, \xi) \middle| 0° < \theta < 180°,\ \xi_{\min} \le \xi \le \xi_{\max}\right\}, \tag{17}$$

the complete energy landscape $\tilde{E}(\theta, \xi)$ can be constructed. These landscapes reveal how the distinct morphological factors, i.e., ρ_s and H/r_0, affect the wetting behavior underlying the Cassie–Wenzel transition by exposing the full spectrum of possible wetting states—including both equilibrium and transition states [Fig. 1(f)]. The equilibrium state corresponds to a stable or metastable wetting state and serves as a quantitative measure of wettability (see Sec. III A). It is identified by locating the minimum of $\tilde{E}(\theta, \xi)$ within the domain, in accordance with the principle of energy minimization,

$$\min\left\{\tilde{E}(\theta, \xi) \middle| 0° < \theta < 180°,\ \xi_{\min} \le \xi \le \xi_{\max}\right\}. \tag{18}$$

Beyond the equilibrium states, the transition state, which appears as a saddle point on the energy landscape, plays a crucial role in describing the Cassie–Wenzel transition pathway. In particular, they are central for quantifying the minimum energy barrier associated with the Cassie–Wenzel transition, as well as the corresponding static friction arising from such a barrier (see Secs. III B and III C). The saddle points can be determined by jointly solving the stationary conditions $\partial\tilde{E}/\partial\theta = 0$ and $\partial\tilde{E}/\partial\xi = 0$, along with a detailed examination of the energy landscape.

B. Energetic considerations for assuming a planar liquid–gas interface within surface defects

We introduce the local contact angle θ_b to characterize the morphology of the liquid–gas interface at an arbitrary position ξ within surface defects. As illustrated schematically in Fig. 2(a), $\theta_b = 0^\circ$ corresponds to a planar interface (blue solid line), $\theta_b > 0^\circ$ to a concave interface (red dashed line), and $\theta_b < 0^\circ$ to a convex interface (red dashed-dotted line). This allows us to construct an interfacial energy landscape as a function of θ and θ_b, with ξ fixed at any value within its admissible range to isolate the contribution of the liquid–gas interface curvature, characterized by θ_b, to the total interfacial energy. This approach avoids additional complexity arising from variations in the liquid–solid contact area and permits a clear thermodynamic assessment of the planar-interface assumption.

For $\theta_b \neq 0^\circ$, the total interfacial energy of the system reads

$$E = \gamma_{lg} D_0 + (\gamma_{sl} - \gamma_{sg})\xi\pi(R\sin\theta)^2 + \gamma_{lg}\sum_{i=1}^{n} D_i. \tag{19}$$

Here, the first term denotes the liquid–gas interfacial energy of the droplet's cap. Based on the standard surface area formula for a spherical cap, this term can be expressed as $\gamma_{lg} 2\pi R^2(1-\cos\theta)$. The second term denotes the interfacial energy change associated with replacing the solid–gas interface by the solid–liquid interface within the wet region, where ξ is a constant chosen arbitrarily within the interval $[\xi_{\min}, \xi_{\max}]$. The third term denotes the liquid–gas interfacial energy contributed by the curved menisci located at the apexes of surface defects. Since $\theta_b \neq 0^\circ$, the liquid–gas interfaces at the defect apexes are modeled as spherical caps, one per wet defect. The total interfacial area contributed by these menisci takes the closed form,

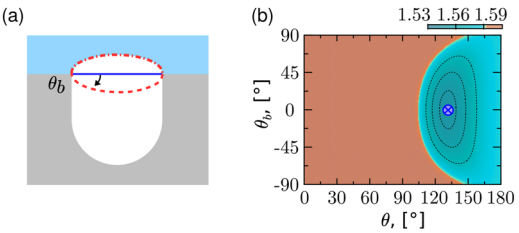

FIG. 2. (a) Definition of the local contact angle θ_b; the lines represent three possible morphologies of the liquid–gas interface pinned at surface defects: planar (blue solid line), convex (red dashed-dotted line), and concave (red dashed line). (b) The energy landscape $\tilde{E}(\theta, \theta_b)$ with the Young's contact angle $\theta_Y = 120^\circ$, the structural design parameter $H/r_0 = 1$, and the average surface defect density $\rho_s = 1 \times 10^5/\text{mm}^2$. The global minimum (blue cross) in the energy landscape occurs at $\theta_b = 0^\circ$, indicating that the planar liquid–gas interface beneath the droplet is energetically favored.

$\sum_{i=1}^{n} D_i = 2\pi(r_s/\sin\theta_b)^2(1-\cos\theta_b)\rho_s\pi(R\sin\theta)^2$, where D_i is the liquid–gas interfacial area at the top of the i-th defect, and the summation includes all n wet defects. Collecting all the contributions and incorporating the volume constraint of Eq. (6), we obtain the dimensionless total interfacial energy in the following form:

$$\tilde{E}(\theta, \theta_b; \xi) = \frac{2 - \eta\xi\cos\theta_Y + 2\eta\psi(1-\cos\theta_b)}{(1-\cos\theta)^{1/3}(2+\cos\theta)^{2/3}}, \tag{20}$$

where $\eta = 1 + \cos\theta$ and $\psi = \rho_s\pi(r_s/\sin\theta_b)^2$. In the limited case $\theta_b = 0^\circ$, the liquid–gas interfaces at the defect apexes are flat, and the system reduces to a special form of the general model described in Sec. II A, where the liquid resides within the surface defect. Accordingly, we fix ξ in Eq. (13) at an arbitrary value within its allowed range, which gives the dimensionless total interfacial energy of the system as

$$\tilde{E}(\theta; \xi) = \frac{2 - (1+\cos\theta)(\xi\cos\theta_Y - \rho_s\pi r_s^2)}{(1-\cos\theta)^{1/3}(2+\cos\theta)^{2/3}}. \tag{21}$$

By systematically sampling $\tilde{E}$ over a grid within the domain of the equation system formed by Eqs. (20) and (21),

$$\Lambda = \{(\theta, \theta_b) \mid 0^\circ < \theta < 180^\circ, -90^\circ < \theta_b < 90^\circ\}, \tag{22}$$

we construct the energy landscape $\tilde{E}(\theta, \theta_b)$, which captures the full range of energetically accessible meniscus morphologies beneath the droplet under the constraint ξ, and thereby determine the corresponding equilibrium states. Figure 2(b) presents the energy landscape obtained under the parameter setting $\theta_Y = 120^\circ$, $H/r_0 = 1$, and $\rho_s = 1 \times 10^5/\text{mm}^2$, serving as a representative example. The landscape exhibits a unique minimum at $\theta_b = 0^\circ$ across the full range of θ, indicating that the liquid–gas interface beneath the droplet is planar at equilibrium. This finding validates our planar interface assumption: any deviation from flatness increases the system's energy, making curved meniscus morphologies beneath the droplet energetically unfavorable. Furthermore, the Young–Laplace equation[42,43] dictates that the mean curvature of the liquid–gas interface within the surface defects must equal that of the capped droplet–gas interface. Given that the characteristic radii of these two interfaces differ by several orders of magnitude, only a flat meniscus can satisfy this curvature equality. This constraint on the interface is consistent with our planar interface assumption. However, this assumption is valid under the following two conditions: (i) the meniscus evolves sufficiently slowly ($\text{We} \ll 1$) to be regarded as residing at a fixed position ξ within the defect at each instant, and (ii) the system is pressure-dominated, with the liquid–gas interface of the macroscopic droplet cap treated as a free interface. Here, the Weber number is defined as $\text{We} = \rho v^2 r_s/\gamma_{lg}$, where v is the characteristic velocity of the meniscus.

When the system is governed by both chemical and mechanical equilibrium and the shape of the macroscopic droplet cap is fixed, previous studies[20,24,25] indicate that the meniscus beneath the droplet develops a finite curvature. In this case, maintaining chemical equilibrium requires an additional constraint, which can be interpreted as an extra thermodynamic force. This additional force leads to a modified mechanical equilibrium, giving rise to the so-called modified Laplace equation in Ref. 24.

III. RESULTS AND DISCUSSION

A. Wettability

Wettability is commonly characterized by the apparent contact angle of a droplet in its equilibrium state on a solid surface. Accordingly, assessing the influence of H/r_0 on wettability amounts to analyzing its effect on the equilibrium contact angle. In this section, we first examine how H/r_0 governs the equilibrium wetting state by shifting the minimum of the energy landscape $\tilde{E}(\theta, \xi)$. Figure 3 presents the two representative energy landscapes illustrating how the profile evolves with varying H/r_0. In panels (a)–(c), the global minimum is located at $\xi_{\max}$ (type A) with $\theta_Y = 95^\circ$ and $\rho_s = 1 \times 10^5/\text{mm}^2$, whereas in panels (d)–(f), the global minimum appears at $\xi_{\min}$ (type B) with $\theta_Y = 120^\circ$ and $\rho_s = 1 \times 10^5/\text{mm}^2$. In type A, two local minima consistently exist in the energy landscape for all values of H/r_0, located at $\xi_{\min}$ and $\xi_{\max}$, corresponding to the Cassie and Wenzel states, which are associated with the equilibrium apparent contact angles θ_C and θ_W, respectively. The global minimum occurs at $\xi_{\max}$, indicating that the Wenzel state is energetically favored. As H/r_0 increases, the position of the local minimum at $\xi_{\min}$ remains unchanged, while the global minimum at $\xi_{\max}$ progressively shifts toward higher θ values [see Figs. 3(a)–3(c)]. This implies that θ_C is nearly insensitive to H/r_0, whereas θ_W increases with increasing H/r_0. In contrast, type B exhibits a qualitatively different behavior. At small values of H/r_0, the energy landscape features two local minima at $\xi_{\min}$ and $\xi_{\max}$, as in type A, with the global minimum located at $\xi_{\min}$, indicating that the Cassie state is more stable [see Fig. 3(d), where $H/r_0 = 0.5$]. However, unlike type A, increasing H/r_0 causes the local minimum at $\xi_{\max}$ to vanish entirely. The system thus enters a regime where only a single minimum remains at $\xi_{\min}$,

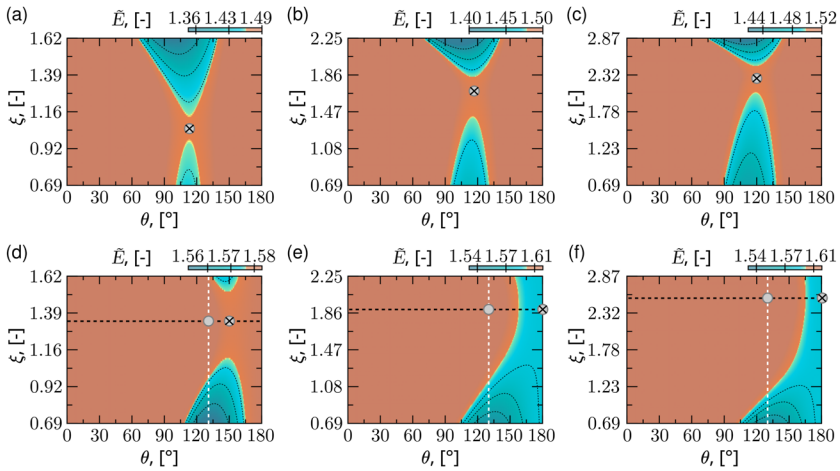

FIG. 3. Energy landscape $\tilde{E}(\theta, \xi)$ governing Cassie–Wenzel transition for different values of the structural design parameter H/r_0. Representative energy landscapes for (a) $H/r_0 = 0.5$, (b) $H/r_0 = 1.5$, and (c) $H/r_0 = 2.5$ showing the global minimum at $\xi_{\max}$ corresponding to the Wenzel state with equilibrium apparent contact angle θ_W, and the local minimum at $\xi_{\min}$ corresponding to the Cassie state with equilibrium apparent contact angle θ_C. Gradual disappearance of the Wenzel state (local minimum at $\xi_{\max}$) with an increase in H/r_0, shown for (d) $H/r_0 = 0.5$, (e) $H/r_0 = 1.5$, and (f) $H/r_0 = 2.5$. The white dashed lines represent the Cassie-to-Wenzel transition pathway assumed in Ref. 41, where the droplet's apparent contact angle is held fixed, and the gray dots mark the highest-energy points along this path. The Young's contact angle θ_Y is 95° in (a)–(c) and 120° in (d)–(f). The average surface defect density is $\rho_s = 1 \times 10^5/\text{mm}^2$ for both panels. The cross symbols denote the saddle point in the energy landscape.

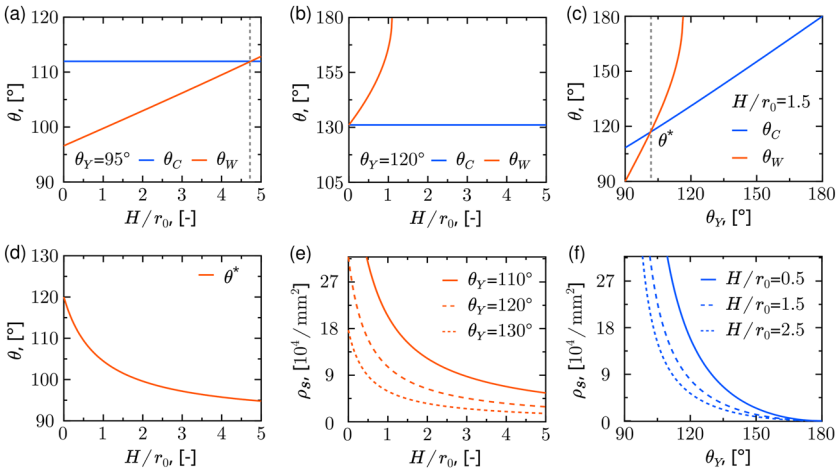

FIG. 4. θ_C [Eq. (23)] and θ_W [Eq. (24)] as functions of H/r_0 for two values of θ_Y with fixed $\rho_s = 1 \times 10^5/\text{mm}^2$: (a) $\theta_Y = 95^\circ$ and (b) $\theta_Y = 120^\circ$. (c) θ_C and θ_W vs θ_Y for fixed $\rho_s = 1 \times 10^5/\text{mm}^2$ and $H/r_0 = 1.5$, where their intersection defines the critical angle θ^* [Eq. (25)]. (d) Monotonic decrease in θ^* with increasing H/r_0. Critical parameter diagrams based on Eq. (26): (e) variation of ρ_s with H/r_0 for different θ_Y, and (f) variation of ρ_s with θ_Y for fixed values of H/r_0. Each curve marks the boundary separating the region where the Wenzel state ceases to exist (above) from the region where both Cassie and Wenzel states coexist (below).

implying that the Cassie state is the only equilibrium configuration accessible to the system.

To further illustrate how the equilibrium contact angles θ_C and θ_W depend on H/r_0, we derive analytical expressions for both angles based on Eq. (18),

$$\cos\theta_C = \left(1 - \rho_s \pi r_0^2\right)\cos\theta_Y - \rho_s \pi r_0^2, \tag{23}$$

$$\cos\theta_W = \left[1 + \rho_s \pi r_0^2 \left(2(H/r_0) + 1\right)\right]\cos\theta_Y. \tag{24}$$

Figures 4(a) and 4(b) plot the values of θ_C and θ_W as functions of H/r_0 based on the analytical expressions in Eqs. (23) and (24). Two representative cases are presented as follows: (a) $\theta_Y = 95^\circ$ with $\rho_s = 1 \times 10^5/\text{mm}^2$ and (b) $\theta_Y = 120^\circ$ with the same ρ_s. From these panels, a straightforward conclusion can be drawn: θ_C remains constant, exhibiting no dependence on H/r_0, as the structural height of the defects varies. In contrast, θ_W increases monotonically with increasing H/r_0, reflecting the enhanced effect of surface roughness on θ_W for hydrophobic surfaces, which is consistent with the predictions of Wenzel's equation. In scenarios where the Cassie and Wenzel states coexist, the decoupling between θ_C and θ_w offers a practical design strategy: by increasing the structural depth, one can enhance θ_W without affecting θ_C.

Previous studies have shown that on hydrophobic surfaces, θ_W can exceed θ_C,[13,33] as illustrated in the region to the right of the gray dashed line in Fig. 4(a) and throughout Fig. 4(b). These works have identified the threshold under which θ_W becomes greater or smaller than θ_C. Here, we further examine how this threshold, denoted as θ^*, depends on H/r_0. By equating the expressions for θ_C and θ_W in Eqs. (23) and (24), we obtain a closed-form relation that defines the critical point in terms of H/r_0 as

$$\cos\theta^* = -\frac{1}{2}\left(\frac{1}{1 + H/r_0}\right). \tag{25}$$

θ^* serves as a boundary separating the regimes of relative wettability: for $\theta_Y > \theta^*$, we find $\theta_W > \theta_C$, whereas for $\theta_Y < \theta^*$, the relation reverses, yielding $\theta_W < \theta_C$. This criterion allows one to determine, for a given set of parameters, which state exhibits a larger apparent contact angle. Figure 4(c) visualizes the threshold by plotting θ_C and θ_W as functions of θ_Y, with $\rho_s = 1 \times 10^5/\text{mm}^2$ and $H/r_0 = 1.5$. The intersection point of the two curves corresponds precisely to the critical angle θ^* defined by Eq. (25). Figure 4(d) then depicts the variation of θ^* with respect to H/r_0, revealing a monotonic decrease in the critical angle as H/r_0 increases. This phenomenon explains the observation in Fig. 4(a), where θ_W is initially smaller than θ_C for low values of H/r_0 but becomes larger once H/r_0 exceeds ~4.74. As θ^* decreases with increasing H/r_0, when it drops below 95°, $\theta_Y = 95^\circ$ shifts from being smaller than θ^* to exceeding it, thereby moving the system from the regime $\theta_W < \theta_C$ to $\theta_W > \theta_C$. Note that by adjusting H/r_0, one can systematically control θ^*, enabling precise manipulation of droplet wetting by determining whether the Wenzel contact angle exceeds the Cassie contact angle under the same θ_Y, which is crucial for the design of engineered surfaces with tailored wettability.

The above comparison relies on the assumption that both the Cassie and Wenzel states are locally stable; however, the energy landscapes in Figs. 3(e) and 3(f) reveal that this is not always the case. In particular, there exists a regime in which the Wenzel state ceases to be a local minimum in the energy landscape, rendering it physically inaccessible. In such a case, the Cassie state becomes the only stable configuration. To identify the condition under which the Wenzel state vanishes, we introduce a practical criterion, $\theta_W = 180^\circ$ marks the threshold for the existence of the Wenzel state. This criterion is motivated by the observation in Fig. 4(b), where θ_W increases with H/r_0 and ultimately approaches 180°; beyond this point, the Wenzel state no longer exists. Substituting $\cos\theta_W = -1$ into Eq. (24), we derive an expression that defines this critical condition,

$$\rho_s\left[2\left(\frac{H}{r_0}\right) + 1\right] = \frac{-1/\cos\theta_Y - 1}{\pi r_0^2}. \tag{26}$$

From Eq. (26), it is evident that under a given r_0, the critical condition is primarily governed by three parameters: ρ_s, H/r_0, and θ_Y. Figure 4(e) depicts the variation of ρ_s with H/r_0 under different θ_Y, while Fig. 4(f) depicts its dependence on θ_Y for fixed values of H/r_0, both derived from Eq. (26). Each curve represents the locus of critical parameter sets at a given θ_Y or H/r_0, dividing the figure into two distinct regions: the area above each curve corresponds to conditions where the Wenzel state no longer exists and the system has the Cassie state as the sole equilibrium configuration; below the curve, both the Cassie and Wenzel states remain locally stable. This critical parameter diagram offers practical design guidance: once any one of the three parameters—ρ_s, H/r_0, or θ_Y—is specified, the corresponding values of the other two can be selected to ensure that the Wenzel state is eliminated, leaving the Cassie state as the only stable configuration. This facilitates the rational design of surfaces that are engineered to sustain Cassie-type wetting without transitioning to the Wenzel state.

B. Energy barrier

In our previous work,[33] we proposed a quantitative definition of the minimum energy barrier associated with the Cassie–Wenzel transition by identifying the transition state along the minimum energy path on the energy landscape—in particular, the saddle point, highlighted by the black cross in Fig. 3. This energy barrier is quantitatively defined as

$$\Delta\tilde{E}_C = \tilde{E}(\theta_S, \xi_S) - \tilde{E}(\theta_C, \xi_{\min}), \tag{27}$$

$$\Delta\tilde{E}_W = \tilde{E}(\theta_S, \xi_S) - \tilde{E}(\theta_W, \xi_{\max}), \tag{28}$$

where $\Delta\tilde{E}_C$ and $\Delta\tilde{E}_W$ denote the energy barriers of Cassie-to-Wenzel and Wenzel-to-Cassie transitions, respectively. $\tilde{E}(\theta_C, \xi_{\min})$, $\tilde{E}(\theta_S, \xi_S)$, and $\tilde{E}(\theta_W, \xi_{\max})$ denote the dimensionless interfacial energies of the Cassie state, the transition state (saddle point), and the Wenzel state, respectively. The transition state on the energy landscape corresponds to an unstable intermediate configuration that separates the Cassie and Wenzel basins and represents a critical configuration that defines the lowest-energy pathway for the system to escape from one basin of attraction to another. As the highest point along the minimum energy path, it defines the energy threshold that must be overcome for the transition to proceed. Accordingly, the energy barrier, defined as the energy difference between the equilibrium and transition states, quantifies the minimum energy required to overcome this threshold. For a 1 μl water droplet, the barrier is on the order of 10^{-9} J, much larger than $k_B T$ at room temperature

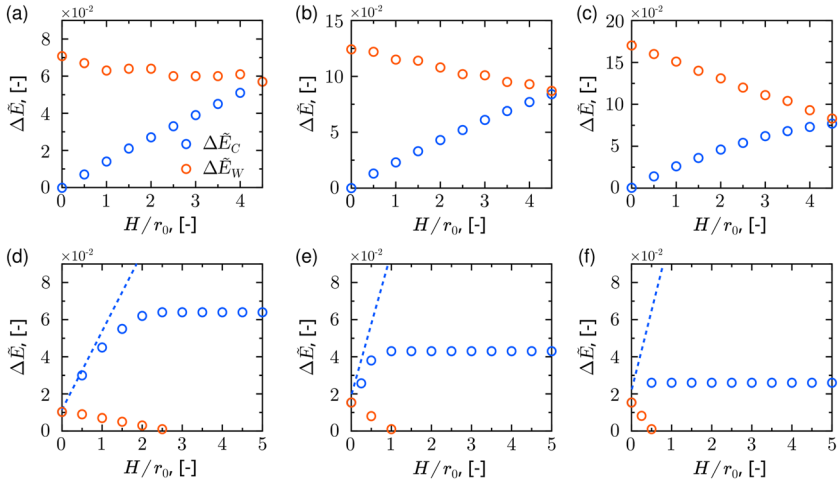

FIG. 5. Energy barriers for the Cassie-to-Wenzel transition, $\Delta\tilde{E}_C$ [Eq. (27)], and the Wenzel-to-Cassie transition, $\Delta\tilde{E}_W$ [Eq. (28)], as functions of H/r_0 for different θ_Y and ρ_s. Panels (a)–(c) correspond to $\theta_Y = 95°$ with $\rho_s = 5\times10^4/\text{mm}^2$, $\rho_s = 1\times10^5/\text{mm}^2$, and $\rho_s = 1.5\times10^5/\text{mm}^2$, respectively. Panels (d)–(f) show the corresponding results for $\theta_Y = 120°$ with the same ρ_s values. In panels (d)–(f), the blue dashed lines indicate $\Delta\tilde{E}_C$ computed according to the approach in Ref. 41.

($T \approx 298$ K), indicating that thermal fluctuations alone cannot surmount it. In this context, the barrier governs the long-term stability of the Cassie and Wenzel states against external perturbations.

Figure 5 provides representative examples illustrating how the energy barriers vary with H/r_0. Panels (a)–(c) correspond to type A for $\theta_Y = 95°$ with $\rho_s = 5\times10^4/\text{mm}^2$, $\rho_s = 1\times10^5/\text{mm}^2$, and $\rho_s = 1.5\times10^5/\text{mm}^2$, whereas panels (d)–(f) correspond to type B for $\theta_Y = 120°$ with the same ρ_s values. As depicted in both panels, the energy barrier of the Wenzel-to-Cassie transition, $\Delta\tilde{E}_W$, exhibits a monotonic dependence on H/r_0, with a pronounced maximum occurring at the smallest values of H/r_0. This behavior remains robust across different values of ρ_s, indicating its generality. The presence of a maximum suggests the existence of an optimal H/r_0 that maximizes the energetic stability of the Wenzel state. However, optimizing H/r_0 alone is insufficient, as the height of the energy barrier is strongly influenced by ρ_s. In particular, the peak barrier increases with increasing ρ_s for type A and type B. This unified behavior across different values of θ_Y highlights the coupled interplay between H/r_0 and ρ_s, implying that the effective stabilization of the Wenzel state requires a generalizable surface design strategy for different wetting regimes. For both type A and type B, increasing ρ_s is beneficial, as it raises the energy barrier and, thus, makes the transition to the Cassie state less accessible. In this context, the combination of a reduced H/r_0 and an elevated ρ_s serves to significantly enhance the energy stability of the Wenzel state.

While $\Delta\tilde{E}_W$ follows a universal trend with H/r_0 in both type A and type B, the behavior of $\Delta\tilde{E}_C$ differs markedly. Its dependence on H/r_0 is type-specific, reflecting the distinct stability characteristics of the Cassie state in different wetting regimes. In type A, $\Delta\tilde{E}_C$ shows a persistent upward trend as H/r_0 increases, and no sign of saturation is observed within the examined range. This continued growth implies that taller surface features can increasingly hinder the onset of the Wenzel state, offering an effective means to reinforce the Cassie configuration. Differently, under type B conditions, $\Delta\tilde{E}_C$ initially grows with increasing H/r_0, but this rise gradually slows and eventually plateaus beyond a threshold H/r_0. Once this saturation point is reached, further increasing pillar height brings no additional energy benefit in suppressing the transition. Crucially, this plateau coincides with the disappearance of the Wenzel solution. This transition from bistability to energy exclusivity marks a sharp contrast to type A, where both Cassie and Wenzel states remain accessible across a broad parameter (e.g., H/r_0) range. These distinctions have direct implications for surface design. In type A scenarios, maximizing H/r_0 remains an effective strategy to elevate the energy barrier and thereby prolong the Cassie state's persistence. In contrast, for type B surfaces, the focus shifts to identifying the critical structural height beyond which the Cassie state becomes intrinsically stable and immune to collapse.

The emergence of the plateau in type B can be traced to a geometric constraint inherent to the saddle-point configuration. As H/r_0 increases, the saddle-point contact angle approaches its upper bound of 180° [see Figs. 3(d)–3(f)]. Once this limit is reached, a further increase in H/r_0 no longer alters the saddle-point contact angle and the corresponding energy. At this stage, the energy of the Cassie state also ceases to depend on H/r_0, rendering the energy cost associated with the Cassie-to-Wenzel transition insensitive to additional structural height. This geometric constraint, therefore, sets a natural upper bound on the barrier in type B and explains the onset of the observed plateau. In our approach, the droplet's apparent contact angle is allowed to vary during the transition, and its value at each step is obtained from energy minimization, which yields the saddle-point geometries shown in Fig. 3. An alternative viewpoint[41] assumes that the apparent contact angle remains fixed throughout the transition. The resulting pathway is illustrated by the white dashed lines in Figs. 3(d)–3(f), with the gray dots marking the highest-energy points. Since the geometric constraint associated with the saddle-point configuration is removed in this scenario, the maximum energy along this path increases linearly with H/r_0. Consequently, the Cassie-to-Wenzel barrier also grows linearly, as indicated by the blue dashed lines in Figs. 5(d)–5(f).

C. Static friction

From a microscopic (atomic- or nanometer-scale) perspective, substrates are intrinsically rough. Given this microscopic roughness, when liquid–gas density asymmetry and fluid–solid van der Waals interactions are taken into account, two distinct microscopic contact angles naturally emerge, as detailed in Ref. 8. The

coexistence of these angles reflects multiple metastable configurations of the droplet, which underlie contact angle hysteresis and provide the origin of the intrinsic static friction. However, in the presence of macroscopic roughness, with characteristic length scales on the micrometer scale or larger, the situation becomes less straightforward, and it remains unclear how this intrinsic static friction manifests at larger length scales. Here, to avoid these ambiguities, we treat the interfaces of surface defects as smooth; microscopic contact angles are not defined on these interfaces, and only a single, well-defined Young's contact angle exists. Intrinsic static friction is, therefore, neglected, and we focus instead on the static friction induced by macroscopic surface structures, which we term the apparent static friction.

A widely accepted formulation for the apparent static friction of a droplet is given by[44–49]

$$F = \omega\gamma_{lg}(\cos\theta_R - \cos\theta_A). \tag{29}$$

Here, ω is the characteristic width of the droplet's contact area with the surface. In the literature, the following two expressions are commonly used: $\omega = 2r_c$[50,51] and $\omega = \pi r_c$,[52] where r_c is the droplet's contact radius [Fig. 1(c)]. The expressions of ω are obtained from an integral of the local apparent static friction along the entire contact line, with a rigorous derivation provided in Appendix D of Ref. 33; the apparent differences arise solely from different conventions for the local apparent static friction direction. θ_A and θ_R are the advancing and receding contact angles, respectively. When contact angle hysteresis is present, θ_A is defined as the maximum observable contact angle at the front edge of the droplet, while θ_R is the minimum observable contact angle at the rear edge.[48] From the energy landscapes of Fig. 3, it is evident that, in the present physical scenario, the apparent contact angle of the transition state, θ_S, represents the largest contact angle that can be realized, whereas θ_C or θ_W corresponds to the smallest realizable contact angle. By definition, θ_S can be identified as θ_A, and θ_C or θ_W as θ_R. Based on these assignments, the general expression for the static friction in Eq. (29) can be expressed as

$$F_C = \omega\gamma_{lg}(\cos\theta_C - \cos\theta_S), \tag{30}$$

$$F_W = \omega\gamma_{lg}(\cos\theta_W - \cos\theta_S). \tag{31}$$

Equation (30) gives the apparent static friction experienced by a droplet in the Cassie state, while Eq. (31) applies to the Wenzel state. By solving the system of equations $\partial\tilde{E}/\partial\theta = 0$ and $\partial\tilde{E}/\partial\xi = 0$, followed by an analysis of the energy landscape, we obtain a closed-form expression for θ_S as

$$\cos\theta_S = \cos\theta_Y - \rho_s\pi r_0^2\left[\cos\ \theta_Y^2 - 2(H/r_0 - 1)\cos\theta_Y + 1\right].$$

We note that $\omega\gamma_{lg}(\cos\theta_{C/W} - \cos\theta_S)$ can also be interpreted as an apparent line tension. This term, resulting from the line integral of the local apparent line tension per unit length along the contact line,[33] characterizes the force required to depin the contact line from underlying defects. For millimetric droplets, its magnitude is typically on the order of 1×10^{-5} N, consistent with the depinning force reported in Ref. 32. In addition to this macroscopic contribution, there exists an intrinsic line tension of typical magnitude[43,53] 1×10^{-11} N, arising from microscopic roughness. Since this intrinsic value is several orders of magnitude smaller than the apparent term in the present regime, it plays no significant role in our formulation.

In experimental practice, direct measurement of static friction is challenging. A classic method to characterize it is to measure the so-called roll-off angle (also known as the tilting angle).[52,54–57] In a typical roll-off experiment, a droplet is gently placed on a solid surface that is gradually tilted. The roll-off angle, denoted by α, is defined as the critical inclination angle at which the droplet begins to move under gravity. The physical basis of this method lies in the force balance at the onset of motion. When the component of gravity along the incline, $\rho gV\sin\alpha$, equals the static friction F, the droplet starts to slide or roll. Therefore, the roll-off angle provides an indirect but reliable measure of the static friction. Based on this force balance, we convert the apparent static friction expressions [Eqs. (30) and (31)] into corresponding predictions for the roll-off angle α,

$$\rho gV\ \sin\alpha_C = \omega\gamma_{lg}(\cos\theta_C - \cos\theta_S), \tag{32}$$

$$\rho gV\ \sin\alpha_W = \omega\gamma_{lg}(\cos\theta_W - \cos\theta_S), \tag{33}$$

where α_C and α_W are the roll-off angles for droplets in Cassie and Wenzel states, respectively. Figure 6 shows the variations of α_C and α_W as functions of H/r_0 for two representative wetting types. For type A [Figs. 6(a)–6(c)], the parameter settings are $\theta_Y = 95^\circ$ with (a) $\rho_s = 5 \times 10^4/\text{mm}^2$, (b) $\rho_s = 1 \times 10^5/\text{mm}^2$, and (c) $\rho_s = 1.5 \times 10^5/\text{mm}^2$. For type B [Figs. 6(d)–6(f)], the settings are $\theta_Y = 120^\circ$ with the same three values of ρ_s. For both wetting types, their evolution with H/r_0 follows exactly the same trend as the corresponding energy barriers. The detailed features of these trends have already been discussed in Sec. III B and are not repeated here.

Despite the overall consistency between the roll-off angles and the corresponding energy barriers, Figs. 6(d)–6(f) reveal an intriguing feature. For the Wenzel state, although α_W generally decreases monotonically with increasing H/r_0, its slope changes abruptly beyond a critical point. This manifests as a discontinuity in the derivative of α_W with respect to H/r_0, indicating a qualitative shift in its sensitivity to structural variations. Interestingly, this critical point coincides with that of α_C transitions from an initial increase to a plateau. In other words, type B exhibits a structural threshold that separates two distinct roll-off regimes, as highlighted by the gray dotted lines in Figs. 6(d)–6(f). To understand the origin of this boundary, we analyze the underlying energy landscape [Figs. 3(d)–3(f)]. By tracing the evolution of the three contact angles involved in the formulation of the roll-off angle, namely, θ_C, θ_W, and θ_S, which restricts the range of accessible contact angle configurations and gives rise to two distinct roll-off regimes. In particular, the plateau in α_C appears once θ_S reaches its geometric upper limit of 180°, beyond which it remains unchanged. After this point, with θ_C remaining constant over the range of H/r_0, the term $(\cos\theta_C - \cos\theta_S)$ in Eq. (32) is constant, and consequently α_C enters a plateau. In contrast, once θ_S reaches the geometric limit, θ_W continues to increase gradually with H/r_0. As θ_W approaches the now-saturated θ_S, the difference $(\cos\theta_W - \cos\theta_S)$ in Eq. (33) gradually diminishes, leading α_W rapidly toward zero. This behavior accounts for the abrupt change in the decreasing rate of α_W beyond the critical point.

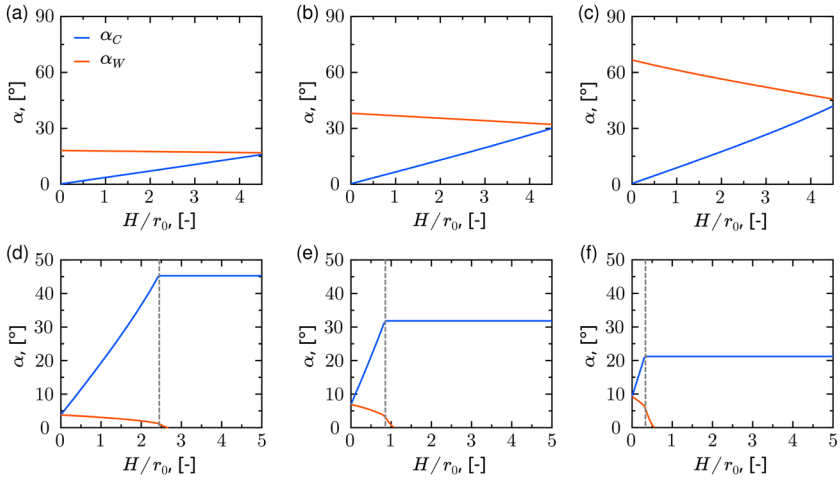

FIG. 6. The roll-off angle of a droplet in the Cassie state, α_C [Eq. (32)], and Wenzel state, α_W [Eq. (33)], vs H/r_0 for different θ_Y and ρ_s. Panels (a)–(c) correspond to $\theta_Y = 95°$ with $\rho_s = 5 \times 10^4/\text{mm}^2$, $\rho_s = 1 \times 10^5/\text{mm}^2$, and $\rho_s = 1.5 \times 10^5/\text{mm}^2$, respectively, while panels (d)–(f) correspond to $\theta_Y = 120°$ with the same ρ_s values. These evaluations confirm that the observed trends in the roll-off angles are not specific to a particular ρ_s.

The geometric constraint—the saturation of θ_S at its maximum permissible value of 180°—is the fundamental cause of the observed bifurcation in roll-off angle behavior. A similar phenomenon appeared in our previous work,[33] where α_C and α_W were analyzed as functions of $\xi_{\min}$. That work primarily aimed to validate our theoretical formulation against experimental data,[52,54] which only covered the rising branch; therefore, our plots were confined to the same interval, and the bifurcation was not explicitly presented. Examination of how the energy landscape evolves with $\xi_{\min}$ is an effective way to reveal the mechanism behind this behavior, explaining why the roll-off angles initially increase and, subsequently, decrease with growing $\xi_{\min}$. Considering the definition $\xi_{\min} = 1 - \rho_s \pi r_0^2$, when r_0 is fixed, $\xi_{\min}$ is solely controlled by ρ_s, increasing as ρ_s decreases. We, therefore, present representative examples of the energy landscapes with different ρ_s to illustrate the evolution of the energy landscape with $\xi_{\min}$, as depicted in Fig. 7. The parameters are set as $\theta_Y = 120°$ and $H/r_0 = 1$, with (a) $\rho_s = 5 \times 10^4/\text{mm}^2$, (b) $\rho_s = 1 \times 10^5/\text{mm}^2$, and (c) $\rho_s = 2 \times 10^5/\text{mm}^2$. For the small $\xi_{\min}$ (corresponding to large ρ_s), θ_S is constrained by its geometric upper bound of 180°, while θ_C and θ_W decrease as $\xi_{\min}$ increases (or equivalently, as ρ_s decreases). Consequently, the differences $(\cos\theta_C - \cos\theta_S)$ and $(\cos\theta_W - \cos\theta_S)$ enlarge [see Figs. 7(c) → 7(b)], resulting in an increase in α_C and α_W. As $\xi_{\min}$ continues to increase (i.e., as ρ_s continues to decrease), θ_S departs from its geometric limit. Owing to its high sensitivity to ρ_s, even a slight reduction in ρ_s causes a rapid drop in θ_S, whereas θ_C and θ_W decrease only modestly over the same interval [see Figs. 7(b) → 7(a)]. As a result, the differences $(\cos\theta_C - \cos\theta_S)$ and $(\cos\theta_W - \cos\theta_S)$ shrink quickly, giving rise to the stage where α_C and α_W decrease with further increasing $\xi_{\min}$. This analysis confirms that the non-monotonic variation of α_C and α_W with $\xi_{\min}$ stems from the saddle-point geometric constraint, which governs how surface morphological factors (e.g., ρ_s and H/r_0) affect the roll-off angle and, equivalently, the static friction.

Figures 8(a) and 8(b) reproduce the rising branch of α_C and α_W against $\xi_{\min}$ as reported in our previous work.[33] Figures 8(c)–8(f) illustrate the decreasing stage of α_C and α_W with respect to $\xi_{\min}$. Panels (c) and (d) present the type A results for $\theta_Y = 95°$ with $H/r_0 = 0.5$ and $H/r_0 = 1.5$, while panels (e) and (f) show the corresponding results for $\theta_Y = 120°$. From these panels, several trends regarding the influence of H/r_0 can be clearly identified. For the behavior of α_C, the maximum value of α_C increases with H/r_0 in both types A and B, indicating that larger H/r_0 enhances the peak static friction before the decline sets in. For the behavior of α_W, in type A, the maximum α_W remains nearly unchanged, reaching values as high as 90°, reflecting a persistently high static friction, while the subsequent decrease becomes more gradual as H/r_0 increases; in type B, α_W is already close to zero due to the early convergence of θ_W toward θ_S, reflecting intrinsically low static friction in this regime. The results in Figs. 6 and 8 establish a direct link between the static friction and the surface morphological factors. This connection provides a clear guideline for structural design: by tailoring H/r_0 and ρ_s, one can either enhance the static friction to stabilize droplets

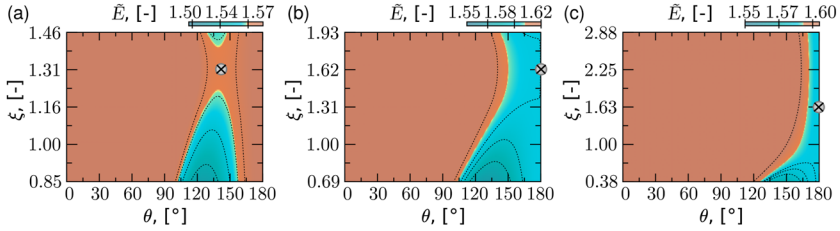

FIG. 7. Energy landscape $\tilde{E}(\theta, \xi)$ for (a) $\rho_s = 5 \times 10^4/\text{mm}^2$, (b) $\rho_s = 1 \times 10^5/\text{mm}^2$, and (c) $\rho_s = 2 \times 10^5/\text{mm}^2$, with saddle points marked by crosses. The contact angle of the saddle point, θ_S, exhibits greater sensitivity to ρ_s than θ_C and θ_W before reaching the geometric upper bound of 180°. Here, $\theta_Y = 120°$ and $H/r_0 = 1$.

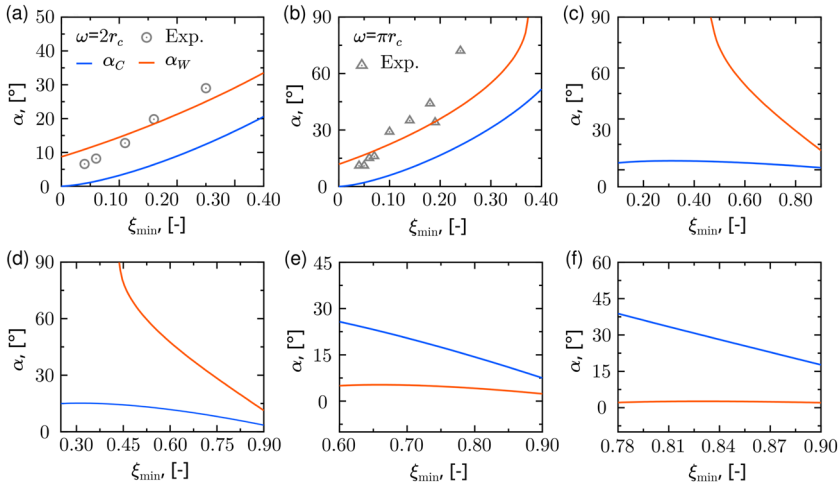

FIG. 8. Rising branch of α_C and α_W vs $\xi_{\min}$ from our previous work, showing comparison with experimental data.[33,52,54] Here, ω denotes the characteristic droplet width and r_c denotes the droplet contact radius: (a) $\omega = 2r_c$, $\theta_Y = 100°$ and (b) $\omega = \pi r_c$, $\theta_Y = 105°$. To illustrate the influence of H/r_0 on the decreasing stage of α_C and α_W as $\xi_{\min}$ increases, we consider two values of H/r_0 for different θ_Y: (c) $H/r_0 = 0.5$ and (d) $H/r_0 = 1.5$ for $\theta_Y = 95°$ and (e) $H/r_0 = 0.5$ and (f) $H/r_0 = 1.5$ for $\theta_Y = 120°$.

or reduce it to facilitate droplet mobility. In particular, two distinct regimes emerge. In the rising branch, increasing H/r_0 and ρ_s drives θ_S toward its geometric upper bound, enlarging $(\cos\theta_{C/W} - \cos\theta_S)$ and, thus, strengthening static friction. In the decreasing branch, reducing H/r_0 and ρ_s allows θ_S to depart from saturation, rapidly weakening static friction and facilitating droplet release.

IV. CONCLUSION

In this work, we have systematically explored how the key structural design parameter, H/r_0 (the ratio of the height H to the radius r_0 of the cylindrical part of defects), influences the Cassie–Wenzel transition, both individually and in conjunction with surface defect density, ρ_s. By using our previously developed theoretical framework, we constructed bivariate free energy landscapes in terms of the apparent contact angle θ and the effective liquid–solid contact ratio ξ, enabling a unified analysis of wettability, energy barrier, and static friction across a range of geometrical conditions.

Our results demonstrate that the influence of H/r_0 differs markedly between two different types of transition—namely, type A, where the Wenzel state corresponds to the global energy minimum, and type B, where the Cassie state is energetically most favorable. In particular, in type A, both Cassie and Wenzel states persist across the full range of H/r_0, while in type B, the Wenzel state vanishes beyond a critical value of H/r_0, leaving only the Cassie state as a stable configuration. In this regime, both the energy barrier and static friction (or equivalently, the roll-off angle) converge to unique, well-defined values. Thus, the coupling between H/r_0 and ρ_s enables the identification of a distinct extremal point where $\Delta\tilde{E}_C$ and F_C attain their maximum values. This turning point provides a quantitative criterion for optimal structural tuning. By tracing this behavior back to the energy landscapes, we identify a geometric constraint at the transition state that fundamentally limits the variation of energy and friction beyond the critical point, explaining the saturation behavior observed in both ΔE_C^* and F_C. To our knowledge, this constraint is reported here for the first time.

Collectively, these findings provide not only fundamental insight into the mechanisms governing the Cassie–Wenzel transition but also practical guidance for surface design. By mapping how specific geometric features modulate wettability, energy barriers, and static friction, our model offers predictive control over the stability and reversibility of wetting states, as well as the droplet mobility. This framework paves the way for rational design of textured surfaces with programmable wetting behaviors, enabling targeted engineering of droplet mobility in both natural and technological contexts.

V. OUTLOOK

Our current analysis focuses on the free energy landscape imposed by macroscopic roughness (i.e., surface defects that can be resolved and have characteristic sizes on the micrometer scale or larger), where the droplet size greatly exceeds the characteristic scale of surface defects. Within this description, the Cassie and Wenzel states appear as the local minima and, thus, enter our formulation of static friction. We fully acknowledge that, when the roughness is comparable to the droplet size, additional metastable minima arise. These local minima, rather than the classical Cassie and Wenzel basins, typically govern contact angle hysteresis, as demonstrated in prior work from our group and others.[58–61] Both of the above scenarios are governed by the apparent line tension introduced by macroscopic roughness. In this unified framework, let $\mathbf{x}$ denote the spatial position along the contact line L; the total free energy of the system reads

$$E = E_0 + \oint_L \lambda(\mathbf{x})\, \mathrm{d}L. \tag{34}$$

Here, the first term represents the reference energy of the system on a smooth surface. The second term accounts for the contribution of the apparent line tension to the system's energy, where $\lambda(\mathbf{x})$ is the local apparent line tension depending on the local contact angle $\theta(\mathbf{x})$ (e.g., advancing or receding contact angles),[33,62] and $\mathrm{d}L$ represents an infinitesimal contact-line element. However, we only consider macroscopic roughness in this model, while microscopic roughness is not included. Incorporating the effect of microscopic roughness, we expect additional minima beyond the classical Cassie and Wenzel basins in our multiscale setting, which cannot be captured by conventional MD simulations. This consideration motivates two

directions for future work. One approach is to include the microscopic roughness effect via an energy contribution proportional to the contact line length L, arising from the intrinsic line tension. Minimization of the total energy, including this term, could produce additional metastable states. However, the precise relationship between apparent line tension and intrinsic line tension remains unclear; currently, a definitive expression for the total free energy including both contributions is unavailable. Alternatively, the microscopic roughness effect can be captured by specifying the fractions of liquid penetrating into the solid beneath the droplet and gas, denoted as ϕ_l and ϕ_g, respectively.[8,43] This alteration renders the wall free energy densities, γ_{sl} and γ_{sg}, functions of ϕ_l and ϕ_g,

$$\gamma_{sl} = \gamma(\phi_l), \quad \gamma_{sg} = \gamma(\phi_g). \tag{35}$$

Substituting Eq. (35) into the energy function of Eq. (34), a new energy function including macroscopic and microscopic roughness contributions is obtained. Minimization of this combined energy may give rise to multiple metastable states. Both strategies thus lead to new energy minima beyond the classical Cassie and Wenzel basins, which can be interpreted in terms of advancing and receding contact angles, providing a more detailed understanding of static friction.

ACKNOWLEDGMENTS

L.B. acknowledges the funding from the China Scholarship Council (CSC). F.W. acknowledges the funding from the VirtMat project "VirtMat P09: Wetting Phenomena" of the Helmholtz Association as part of the program "MSE—Materials Science and Engineering" (Grant No. 43.31.01).

AUTHOR DECLARATIONS

Conflict of Interest

The authors have no conflicts to disclose.

Author Contributions

Lisen Bi: Conceptualization (supporting); Formal analysis (lead); Investigation (equal); Methodology (equal); Validation (equal); Writing – original draft (lead). **Fei Wang**: Conceptualization (lead); Investigation (equal); Methodology (equal); Supervision (equal); Validation (equal); Writing – original draft (supporting); Writing – review & editing (lead). **Britta Nestler**: Project administration (lead); Resources (lead); Supervision (equal); Writing – review & editing (equal).

DATA AVAILABILITY

The data that support the findings of this study are available from the corresponding author upon reasonable request.

REFERENCES

[1] F. Wang, Y. Wu, and B. Nestler, Adv. Mater. **35**, 2210745 (2023).
[2] F. Geyer, M. D'Acunzi, A. Sharifi-Aghi, A. Saal, N. Gao, A. Kaltbeitzel, T.-F. Sloot, R. Berger, H.-J. Butt, and D. Vollmer, Sci. Adv. **6**, eaaw9727 (2020).
[3] Y. Hou, Y. Chen, Y. Xue, Y. Zheng, and L. Jiang, Langmuir **28**, 4737–4743 (2012).
[4] Y. Li, L. Han, X. Zhang, N. Zhang, and D. Tian, Adv. Mater. **29**, 1703802 (2017).
[5] A. B. D. Cassie and S. Baxter, Trans. Faraday Soc. **40**, 546 (1944).
[6] R. N. Wenzel, Ind. Eng. Chem. **28**, 988 (1936).
[7] T. Young, Phil. Trans. R. Soc. **95**, 65 (1805).
[8] F. Wang and B. Nestler, Phys. Rev. Lett. **132**, 126202 (2024).
[9] H. Y. Erbil, Langmuir **36**, 2493–2509 (2020).
[10] R. Blossey, Nat. Mater. **2**, 301–306 (2003).
[11] X. Dai, B. B. Stogin, S. Yang, and T.-S. Wong, ACS Nano **9**, 9260–9267 (2015).
[12] P. G. de Gennes, F. Brochard-Wyart, and D. Quéré, *Capillarity and Wetting Phenomena* (Springer, 2003).
[13] A. Lafuma and D. Quéré, Nat. Mater. **2**, 457–460 (2003).
[14] C. Ishino, K. Okumura, and D. Quéré, Europhys. Lett. **68**, 419 (2004).
[15] M. Liu and L. Jiang, Adv. Funct. Mater. **20**, 3753–3764 (2010).
[16] E. Bormashenko, Y. Bormashenko, T. Stein, G. Whyman, and E. Bormashenko, J. Colloid Interface Sci. **311**, 212–216 (2007).
[17] Y. Cao, S. Jana, X. Tan, L. Bowen, Y. Zhu, J. Dawson, R. Han, J. Exton, H. Liu, G. McHale, N. S. Jakubovics, and J. Chen, Langmuir **36**, 13396–13407 (2020).
[18] G. Liu, L. Fu, A. V. Rode, and V. S. J. Craig, Langmuir **27**, 2595–2600 (2011).
[19] R. Hensel, A. Finn, R. Helbig, S. Killge, H.-G. Braun, and C. Werner, Langmuir **30**, 15162–15170 (2014).
[20] P. Lv, Y. Xue, Y. Shi, H. Lin, and H. Duan, Phys. Rev. Lett. **112**, 196101 (2014).
[21] M. Xu, G. Sun, and C. j. Kim, Phys. Rev. Lett. **113**, 136103 (2014).
[22] Y. Xiang, S. Huang, P. Lv, Y. Xue, Q. Su, and H. Duan, Phys. Rev. Lett. **119**, 134501 (2017).
[23] Y. Xiang, S. Huang, T.-Y. Huang, A. Dong, D. Cao, H. Li, Y. Xue, P. Lv, and H. Duan, Proc. Natl. Acad. Sci. **117**, 2282–2287 (2020).
[24] A. Giacomello, M. Chinappi, S. Meloni, and C. M. Casciola, Phys. Rev. Lett. **109**, 226102 (2012).
[25] A. Giacomello, S. Meloni, M. Müller, and C. M. Casciola, J. Chem. Phys. **142**, 104701 (2015).
[26] Y. Liu and X. Zhang, J. Chem. Phys. **146**, 164704 (2017).
[27] T. Koishi, K. Yasuoka, S. Fujikawa, T. Ebisuzaki, and X. C. Zeng, Proc. Natl. Acad. Sci. **106**, 8435–8440 (2009).
[28] Y. Zhang, X. Gu, Y. Wang, X. Xu, and L. Zhang, Soft Matter **21**, 2729–2737 (2025).
[29] E. Bormashenko, Adv. Colloid Interface Sci. **222**, 92–103 (2015).
[30] G. Whyman, E. Bormashenko, and T. Stein, Chem. Phys. Lett. **450**, 355–359 (2008).
[31] G. Whyman and E. Bormashenko, Langmuir **27**, 8171–8176 (2011).
[32] E. Bormashenko, R. Pogreb, G. Whyman, and M. Erlich, Langmuir **23**, 6501–6503 (2007).
[33] L. Bi, F. Wang, and B. Nestler, Phys. Rev. Res. **7**, 043093 (2025).
[34] J. Bico, U. Thiele, and D. Quéré, Colloids Surf. A: Physicochem. Eng. Asp. **206**, 41–46 (2002).
[35] E. Bormashenko, R. Pogreb, T. Stein, G. Whyman, M. Erlich, A. Musin, V. Machavariani, and D. Aurbach, Phys. Chem. Chem. Phys. **10**, 4056–4061 (2008).
[36] F. Wang and B. Nestler, J. Chem. Phys. **154**, 094704 (2021).
[37] J. W. Cahn, J. Chem. Phys. **66**, 3667–3672 (1977).
[38] F. Aurbach, F. Wang, and B. Nestler, J. Chem. Phys. **161**, 164708 (2024).
[39] H. Zhang, H. Zhang, F. Wang, and B. Nestler, J. Chem. Phys. **161**, 194705 (2024).
[40] F. Aurbach, F. Wang, and B. Nestler, J. Chem. Phys. **163**, 034706 (2025).
[41] N. A. Patankar, Langmuir **20**, 7097–7102 (2004).
[42] F. Wang, H. Zhang, Y. Wu, and B. Nestler, J. Fluid Mech. **970**, A17 (2023).
[43] F. Wang, H. Zhang, and B. Nestler, Phys. Rev. Lett. **133**, 246201 (2024).
[44] L. Bi, B. Liu, Z. Zhu, P. E. Theodorakis, H. Hu, and Z. Li, Phys. Fluids **35**, 012015 (2023).
[45] Z. Li, B. Liu, Y. Guo, L. Bi, H. Hu, Z. Tao, R. Li, and P. Theodorakis, Langmuir **40**, 3527–3539 (2024).
[46] B. Liu, Z. Li, L. Bi, P. E. Theodorakis, Y. Liu, J. Song, A. Chen, Z. Zhu, and J. Song, Therm. Sci. Eng. Prog. **40**, 101771 (2023).

[47]C. G. L. Furmidge, J. Colloid Sci. **17**, 309–324 (1962).
[48]H.-J. Butt, R. Berger, J. D. Coninck, and R. Tadmor, Nat. Rev. Phys. **7**, 425–438 (2025).
[49]R. Tadmor, Langmuir **37**, 6357–6372 (2021).
[50]N. Gao, F. Geyer, D. W. Pilat, S. Wooh, D. Vollmer, H.-J. Butt, and R. Berger, Nat. Phys. **14**, 191–196 (2018).
[51]X. Li, P. Bista, A. Z. Stetten, H. Bonart, M. T. Schür, S. Hardt, F. Bodziony, H. Marschall, A. Saal, X. Deng, R. Berger, S. A. L. Weber, and H.-J. Butt, Nat. Phys. **18**, 713–719 (2022).
[52]M. Reyssat and D. Quéré, J. Phys. Chem. B **113**, 3906–3909 (2009).
[53]L. Guillemot, T. Biben, A. Galarneau, G. Vigier, and É. Charlaix, Proc. Natl. Acad. Sci. **109**, 19557–19562 (2012).
[54]C. Lv, C. Yang, P. Hao, F. He, and Q. Zheng, Langmuir **26**, 8704–8708 (2010).
[55]P. Jin, K. Zhao, Z. Blin, M. Allais, T. Mouterde, and D. Quéré, J. Chem. Phys. **158**, 204709 (2023).
[56]X. Li, A. D. Ratschow, S. Hart, and H.-J. Butt, Phys. Rev. Lett. **131**, 228201 (2023).
[57]X. Li, F. Bodziony, M. Yin, H. Marschall, R. Berger, and H.-J. Butt, Nat. Commun. **14**, 4571 (2023).
[58]M. Silvestrini, A. Tinti, A. Giacomello, and C. Brito, Adv. Mater. Interfac. **8**, 2101005 (2021).
[59]M. Nosonovsky and B. Bhushan, Nano Lett. **7**, 2633–2637 (2007).
[60]Y. Wu, H. Zhang, F. Wang, and B. Nestler, Commun. Phys. **8**, 38 (2025).
[61]Y. Wu, F. Wang, S. Ma, M. Selzer, and B. Nestler, Soft Matter **16**, 6115–6127 (2020).
[62]R. Tadmor, Langmuir **20**, 7659–7664 (2004).